

Cite this article as: Zhang Jianguo, Wang Guan, Chen Peng, et al. Mechanical Properties of Truss-like and Extreme Surface-like Point Structures[J]. Rare Metal Materials and Engineering, 2023, 52(12): 4029-4039.  
DOI: 10.12442/j.issn.1002-185X.20230322.

ARTICLE

# Mechanical Properties of Truss-like and Extreme Surface-like Point Structures

Zhang Jianguo<sup>1</sup>, Wang Guan<sup>1</sup>, Chen Peng<sup>1</sup>, Zhao Sheng<sup>1</sup>, Hu Fengling<sup>2,3</sup>, Song Liang<sup>4</sup>, Zhou Qiong<sup>1</sup>, Zhang Ergeng<sup>1</sup>

<sup>1</sup> Shanghai Engineering Research Center of Physical Vapor Deposition (PVD) Superhard Coating and Equipment, School of Mechanical Engineering, Shanghai Institute of Technology, Shanghai 201418, China; <sup>2</sup> Shanghai Geriatric Medical Center, Shanghai 201100, China; <sup>3</sup> Department of Stomatology, Zhongshan Hospital, Fudan University, Shanghai 200032, China; <sup>4</sup> Department of Stomatology, Shanghai Fifth People's Hospital, Fudan University, Shanghai 200240, China

**Abstract:** The design and mechanical properties of porous titanium alloys has become a hot research topic in the biomedical field. Two types of Gyroid minimal surface monolithic structures, i.e. homogeneous and gradient, were designed and prepared by laser selective melting (SLM). By conducting static compression and tensile experiments on them, and comparing them with traditional truss-like cellular structures, the quasi-static compression models of five different lattice structures were established. The mesh division and analysis were carried out through the co-simulation of Hypermesh and ABAQUS. Five types of porous structure failure forms and deformation mechanisms of hollow cubic, G7, bcc, homogeneous Gyroid and gradient Gyroid were analyzed through the observation of stress-strain nephogram, plastic strain nephogram and compression experiment process. The stress-strain curves obtained by simulation were compared with the experimental results. Results show that the simulation method can better predict the maximum compressive strength of different porous structures. The results of compression and tensile experiments show that the maximum tensile properties of Gyroid lattice materials are much higher than those of truss-like structures, and the compressive properties are also superior. Among them, the G-gradient structure has the best overall mechanical properties.

**Key words:** laser selective melting; Ti6Al4V alloy; three-period minimal surface; finite element analysis

At present, porous materials are widely used in aviation, aerospace, machinery, and other fields due to their excellent energy absorption, noise reduction, heat dissipation performance, and light weight. Moreover, due to their low elastic modulus and internal pore connectivity, they also have an important position in the medical field. In biomedical applications, porous materials are used to adjust the characteristics of the implant and to avoid bone resorption around the implant due to uneven stress distribution at the boundary of the bone implant and mismatch in elastic modulus between the bone and the implant, resulting in stress shielding<sup>[1-2]</sup>.

In recent years, due to the progress of additive manufacturing technology and the reduction of large-scale production costs, there are more and more cases of using cellular materials in functional component design<sup>[3-5]</sup>, making

the manufacturing of periodic cellular structures possible. Additive manufacturing (AM), also known as 3D printing, is a technology that uses computer-aided software such as CAD to design 3-dimensional part drawings in advance in a computer, then MAGICS software is used to segment the three-dimensional drawings, convert them into two-dimensional flat surfaces for processing, and then import the models to be printed into a 3D printer for complete processing<sup>[6-9]</sup>. Selective laser melting has excellent manufacturing capabilities for metal structural materials, which can produce complex models with high accuracy, providing a feasible manufacturing method for crystal cell structures<sup>[10-11]</sup>, which has become a mainstream processing and manufacturing technology for medical implants. Murr et al<sup>[12]</sup> from the University of Texas in the United States fabricated porous metal implant Ti6Al4V through SLM technology, and obtained a finished product

Received date: May 29, 2023

Foundation item: 2023 Shanghai Institute of Technology Collaborative Innovation Fund (XTCX2023-18)

Corresponding author: Hu Fengling, Master, Attending Physician, Shanghai Geriatric Medical Center, Shanghai 201100, P. R. China, E-mail: flhu201418@163.com

Copyright © 2023, Northwest Institute for Nonferrous Metal Research. Published by Science Press. All rights reserved.

with better performance than implants manufactured by traditional methods.

Triple periodic minimal surfaces (TPMS) are surfaces that exhibit periodicity in three independent directions in three-dimensional space, with an average curvature of 0 at any point on the surface, which is similar to the average curvature of the human bone trabeculae. TPMS is composed of smooth surfaces, and the model has good continuity, greatly reducing the area of stress<sup>[13-15]</sup>. At the same time, research has found that cell tissue grows faster on curved surfaces than on planar surfaces<sup>[16]</sup>. Therefore, in the field of biomedicine, the study of porous structures such as three periodic minimal curved surfaces has great significance. TPMS is a smooth and continuous surface that can be described mathematically. The TPMS structure model can be accurately modeled through mathematical methods. Processing and manufacturing through additive manufacturing technology, due to its unique structure, is self supporting in the 3D printing process, which is very consistent with the processing technology of additive manufacturing. At the same time, this type of structure has good permeability and high specific surface area, which is conducive to promoting cell attachment, proliferation and differentiation, and has the characteristics of mechanical conduction<sup>[17]</sup>.

So far, the research on porous scaffolds has mainly focused on the homogeneous structure<sup>[18]</sup>. Since different locations of human natural bone have different porosity, they are not a single structure. Therefore, in order to more effectively simulate the characteristics of natural bone, it is necessary to conduct in-depth research on the mechanical properties of regularly gradient porous structures, which can better meet the needs of bone scaffolds. The National University of Dublin, Ireland, studied the microstructure distribution and compression performance of different cell types, and discovered that Trab (5.58 GPa) and TPMS (5.51 GPa) lattices can be comparable to natural bone (0.022–21 GPa) lattices, effectively avoiding the stress shielding effect that often occurs in biomedical implants. Among them, the Trab structure has higher compressive strength and better energy absorption capacity than the TPMS structure<sup>[19]</sup>. Fukuda et al<sup>[20]</sup> studied the effect of porous titanium implants with different apertures prepared by SLM technology on inducing bone tissue growth, and found that porous implants with apertures of 500 and 600  $\mu\text{m}$  can effectively promote bone tissue growth. Zargarion et al<sup>[21]</sup> conducted mechanical tests on three structures, namely cubic octahedron, rhombic dodecahedron and diamond, to investigate the effect of relative density on the fatigue properties of different structures. The results show that the relationship between fatigue strength and fatigue cycles of

$$F(x, y, z) = \sin\left(\frac{2\pi}{a}x\right)\cos\left(\frac{2\pi}{a}y\right) + \sin\left(\frac{2\pi}{a}y\right)\cos\left(\frac{2\pi}{a}z\right) + \sin\left(\frac{2\pi}{a}z\right)\cos\left(\frac{2\pi}{a}x\right) = C \quad (1)$$

where  $a$  represents the size of the single cell,  $c$  controls the volume enclosed by the minimal surface, and  $x$ ,  $y$ , and  $z$  represent the Cartesian coordinate system. The size and porosity of porous structure single cells can be accurately controlled through mathematical expressions. This research

porous structures follows an exponential relationship, and the coefficient depends on the relative density and structure type of the porous structure.

The above studies indicate that topological optimization of porous titanium alloy structure is needed to meet the requirements of long-term use after implantation in human body, and the type and size of crystal cells are the main factors affecting the mechanical properties of implantation<sup>[22]</sup>. In this study, five single-cell structures were designed by means of Computer-Aided Design (CAD) and MATLAB implicit function modeling. Experimental specimens of the five monocellular structures were fabricated by selected laser melting (SLM) and characterized by static compression and tensile tests to obtain stress-strain curves in compression and tension for the five different unicellular structures. The mechanical response of the samples was investigated by varying the number of monolithic cells in the same porosity by means of equal scaling. The uniaxial compression simulations of five different porous structures were carried out using the joint simulation method of Hypermesh and ABAQUS. The stress and plastic strain clouds obtained from the calculation results were compared with the experimental results to investigate the mechanism of compression deformation of these five structures. The maximum compressive strength of the different porous structures was predicted.

## 1 Experiment

### 1.1 Modeling of truss-like lattice structure

Using SolidWorks 2020 (Dassault Systemes, France) to perform commands such as scanning, stretching, and Boolean operations, three cell structures including hollow cubic, G7 and bcc were constructed in units of spatial cubic space, as shown in Fig. 1. By changing the diameter of the support, their porosity was controlled within a range of about 50% per unit cubic space. Then the experimental sample model was obtained by means of replication and array.

It is assumed that all materials are homogeneous, linearly elastic and isotropic. The mesh was calculated with greater accuracy by a second order mesh cell, C3D10M. The cell size was chosen to be 2.5 mm and the error in the stress value was 4.67%, which is less than 5%<sup>[23]</sup> and can be considered as an acceptable compromise.

### 1.2 Construction of G-unit homogeneous and gradient model

The surface morphology of TPMS can be represented by implicit function equations. As shown in Fig.2a, Gyroid is one of the typical three periodic minimal surfaces, and its mathematical expression is:

$$F(x, y, z) = \sin\left(\frac{2\pi}{a}x\right)\cos\left(\frac{2\pi}{a}y\right) + \sin\left(\frac{2\pi}{a}y\right)\cos\left(\frac{2\pi}{a}z\right) + \sin\left(\frac{2\pi}{a}z\right)\cos\left(\frac{2\pi}{a}x\right) = C \quad (1)$$

used MATLAB software to define the function  $\text{fun}=@(x, y, z)$ , applied the Meshgrid function to generate mesh sampling points, and then used the Isosurface function to solve the surface with  $\text{iso}=0$ . Finally, the solved surface is divided into triangle surfaces, and a file in stl format is output to generate a

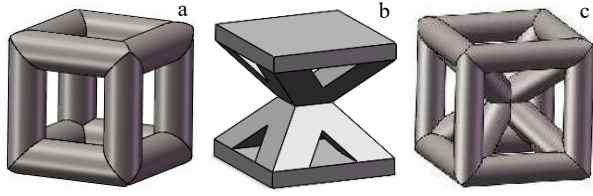


Fig.1 Single cells of three different spatial structures: (a) hollow cube, (b) G7, and (c) bcc

single thin-walled cell with a spatial range of 1 mm×1 mm×1 mm. The method of closing and thickening the section is used to truncate the generated surface using the  $x$ ,  $y$ , and  $z$  planes to make the surface close, which is convenient for 3D printing and finite element simulation of the solid element, as shown in Fig. 2b. Eq. (1) represents the intersection of solid and pore interface,  $F(x, y, z) > C$  represents the solid part,  $F(x, y, z) < C$  represents the pore part, by changing the value of  $C$  can bias the position of the surface so as to control the porosity of the crystal cell, and the calculation formula for porosity is:

$$P = \left(1 - \frac{V}{V_0}\right) \times 100\% \quad (2)$$

where  $V_0$  is the volume of the hexahedron enclosing the unicellular structure,  $V$  is the solid volume of the unicellular structure, and  $P$  is the porosity of the unicellular body. The linear relationship between the value of  $C$  and the porosity is:

$$P = (-0.3477C + 0.5) \times 100\% \quad (3)$$

To achieve a continuous distribution of TPMS porosity, it is achieved by assigning a bias  $C$  about the coordinate function.

$$C = C(x) = kx + b \quad (4)$$

where  $x$  represents the  $x$ -axis direction, and  $k$ ,  $b$  represent the constants controlling the gradient change. The porosity of the

$$F(x, y, z) = \sin\left(\frac{2\pi}{a}x\right)\cos\left(\frac{2\pi}{a}y\right) + \sin\left(\frac{2\pi}{a}y\right)\cos\left(\frac{2\pi}{a}z\right) + \sin\left(\frac{2\pi}{a}z\right)\cos\left(\frac{2\pi}{a}x\right) = 1.15x - 0.5752 \quad (9)$$

A gradient porous structure with a transition from 70% outside porosity to 30% inside porosity with an average porosity of 50% is shown in Fig. 3a, and a porous structure with a mean porosity of 50% is shown in Fig. 3b.

### 1.3 Machining and characterization of porous structural prototypes

According to ISO 13314: 2011, the sample model for compression experiments was designed to be 10 mm×10 mm×15 mm, and tensile experiments were carried out using a dog bone type tensile sample with a square cross-section (6 mm×6 mm×6 mm), and the size of the unicellular structure in the sample model used for the experiments was 1 and 2.5 mm<sup>3</sup>.

This experiment was conducted on an EOSINTM 280 metal 3D printer (EOS, Germany), using Ti6Al4V powder with 25–40 μm in size in an inert argon gas to prepare CAD designed porous structures with TPMS porous structures designed by implicit function parameterisation. Using the pasteboard printing method, the experimental sample was removed from the substrate by wire cutting after the printing was completed, and the rough side was polished. In order to remove the

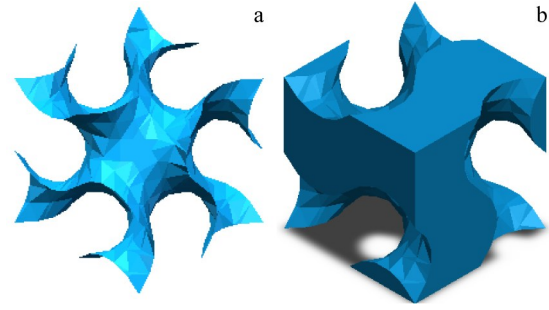


Fig.2 Gyroid of single cell structure: (a) thin-walled structure and (b) rod-shaped structure

outermost ( $x=1$ ) is set as  $P_{out}$ , the porosity of the innermost ( $x=0$ ) is set as  $P_{in}$ ,  $P_{out}$  corresponds to the bias  $C$  as  $C_{out}$ ,  $P_{in}$  corresponds to the bias  $C$  as  $C_{in}$ ,  $k$  and  $b$  are expressed by  $C_{in}$ ,  $C_{out}$ , and Eq. (5) and Eq. (6) are obtained. Eq. (3), Eq. (5) and Eq. (6) are substituted into Eq. (4) to obtain Eq. (7).

$$k = \frac{1}{l} (C_{out} - C_{in}) \quad (5)$$

$$b = C_{in} \quad (6)$$

$$C(x) = \frac{P_{out} - P_{in}}{-0.3477} \frac{x}{l} + P_{in} \quad (7)$$

The gradient change of porosity can be precisely controlled by Eq. (7). In this study, the porous structure with 50% porosity is used as the research object, and a porous gradient model with an average porosity of 50% is designed with  $P_{out}$  of 30% and  $P_{in}$  of 70%. The equation for the bias  $C$  is obtained as follows:

$$C(x) = 1.15x - 0.5752 \quad (8)$$

The gradient model is created in units of 1 mm×1 mm×1 mm and the final equation of the gradient model is obtained as:

unmelted powder from the samples, all samples were cleaned with anhydrous ethanol in an ultrasonic cleaner with ultrasonic oscillation for 30 min. After cleaning and drying, they were placed in sealed bags for storage. Porous samples with 1 mm×1 mm×1 mm and 2.5 mm×2.5 mm×2.5 mm single cells were designed for this experiment, and the samples of bcc, G7 and hollow cubic structures used for quasi-static

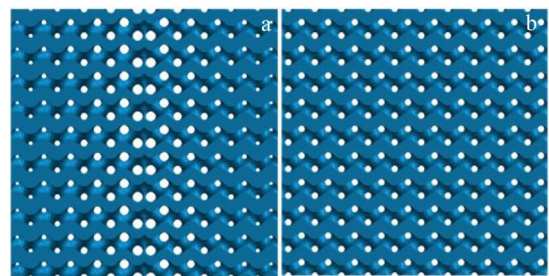


Fig.3 Porous structures with an average porosity of 50%: (a) gradient porous structure and (b) homogeneous porous structure

compression experiments are shown in Fig. 4. The experimental specimens for the homogeneous and gradient Gyroid structures (2.5 mm×2.5 mm×2.5 mm for the single cell on the left and 1 mm×1 mm×1 mm on the right) are shown in Fig.5. Stretched samples of G7, bcc, homogeneous Gyroid and gradient Gyroid as shown in Fig. 6 (all single cells are 1 mm×1 mm×1 mm).

The porosity of the prototype is somewhat different compared to the CAD model, i.e. the porosity of the truss-like dot matrix structure is greater than that of the designed porosity. As shown in Fig.7, the truss-like porous cell structure (hollow cubic, G7, bcc) was observed by SEM. As shown in Fig. 8 the point structure is composed of homogeneous and gradient very small surface Gyroid.

**1.4 Mechanics experiment**

Quasi-static compression and tension experiments were performed in accordance with ISO 13314:2011. Experiments were performed using MTS brand E45.105 series electronic

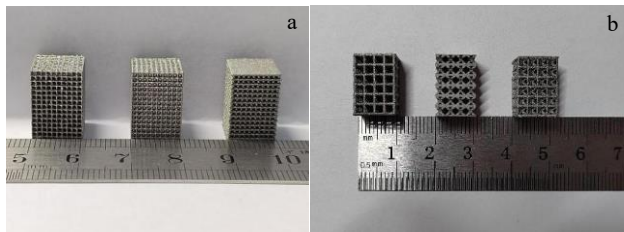


Fig.4 Compression and fatigue test samples of hollow cube, G7 and bcc porous samples: (a) 1 mm×1 mm×1 mm unit cell and (b) 2.5 mm×2.5 mm×2.5 mm unit cell

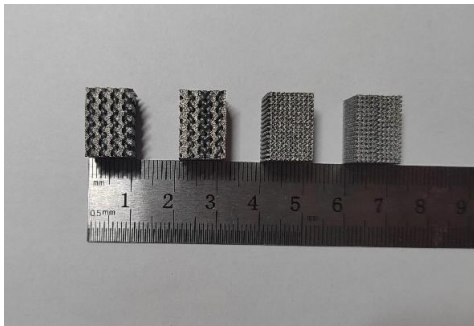


Fig.5 Compression test samples of Gyroid

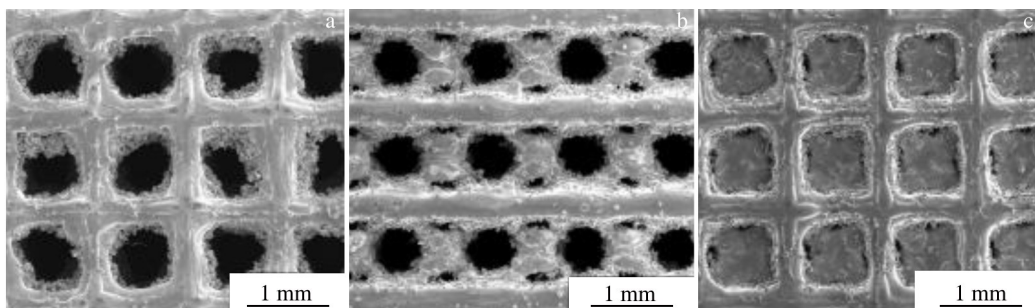


Fig.7 Apparent morphologies of truss type structure sample: (a) hollow cube, (b) G7, and (c) bcc

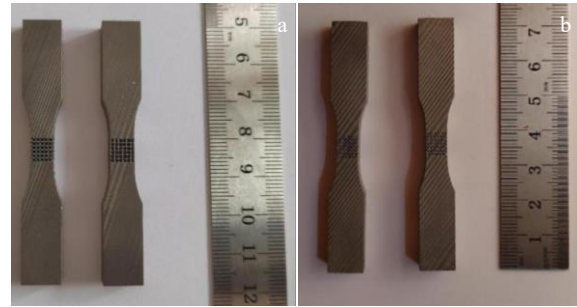


Fig.6 Tensile sample of porous structure: (a) G7 and bcc tensile samples and (b) homogeneous and gradient Gyroid stretched samples

universal testing machine (range: 100 kN). Compression experiments were carried out at room temperature with the compression loading speed set to 0.5 mm/min. The experiments were stopped when the force applied by the machine was less than 50% of the maximum pressure in the compression process. The tensile experiment was carried out at room temperature and the tensile speed was set to 1 mm/min. The test was conducted for the dotted structure consisting of unit cell space size of 1 mm<sup>3</sup>, and the tensile samples of G7, bcc, homogeneous Gyroid structures, and gradient Gyroid porous structures were tested, and their tensile stress-strain curves were plotted by the collected force and displacement data. For the convenience of expression, the homogeneous Gyroid and the Gyroid dotted material with gradient are abbreviated as G homogeneous and G gradient in the follows, respectively.

**1.5 Construction of a quasi-static compression model**

This chapter uses ABAQUS 2020 to carry out model calculations for quasi-static compression of different dotted structures (Fig.9). The model is a 2.5 mm<sup>3</sup> sample consisting of the unicellular body, which has the same size as the experimental sample, and the simulation and analysis process is also consistent with the experimental process. As the strength of the upper and lower planes subjected to compression is much greater than that of the porous material in the actual experiments, these two planes are set as rigid planes in the finite element modelling. The quasi-static compression model consists of three main parts; the middle part is the porous structure, its upper and lower sides are rigid

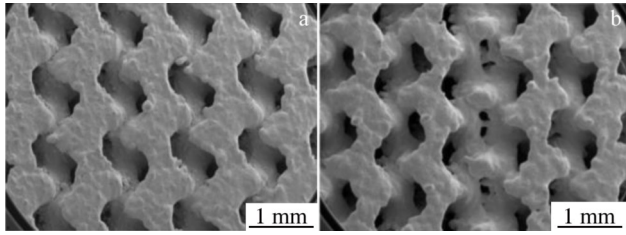


Fig.8 Apparent morphologies of the minimal surface type structure sample: (a) homogeneous Gyroid and (b) gradient Gyroid

planes; the lower rigid plane is a fixed constraint; the upper rigid plane has only one degree of freedom in the compression direction, moving continuously along the compression direction to smooth out the analysis step, and stopping when the compression reaches 20% strain in the porous structure. The porous structure and the rigid planes on the upper and lower sides are universal contacts. During the simulated compression process, the rigid planes on the upper and lower sides are in close contact with the porous structure without gaps, and there are no penetration between the porous structure and the rigid planes, so the normal contact in the universal contact is set as a hard contact and the tangential contact is set as a penalty function.

It should be noted that when constructing the quasi-static compression model, the upper side rigid surface can retain a small gap with the porous material beforehand, and the upper side rigid plane can have a small transition space at the beginning of compression before slowly contacting the porous structure, which can make the contact more stable and reduce the situation of non-convergence of the model calculation. The analysis step used in this simulation is ABAQUS's display dynamics module (ABAQUS/Explicit), which uses a simple algorithm for calculating complex non-linear problems with good convergence. The quasi-static compression models for the five different point structures are shown in Fig.9, where the G homogeneous and G gradient point structures have been meshed in Hypermesh beforehand and imported into ABAQUS due to their complex shapes.

The material used in the porous part of the structure is Ti6Al4V with a theoretical density of  $4.43 \text{ g/cm}^3$ , an elastic modulus of 110 GPa and a Poisson's ratio of 0.33. Homogeneous and gradient Gyroid dot structures are generated by MATLAB stl file, the model is composed of triangular face pieces, so there are many uneven triangular features on the

model. ABAQUS is difficult to automatically mesh them correctly, so professional meshing software Hypermesh is used to mesh them. The model's surface is meshed in 2D, as shown in Fig.10, with G gradient 2D meshing (layer by layer), and after meshing of all faces of the model, the entire surface is free of free edges and T-edges. It is meshed in tetramesh 3D, exported as an inp file and imported into ABAQUS software once the division is complete. The number of meshes for the G homogeneous and G gradient models is 604 128 and 509 787, respectively.

## 2 Results and Discussion

### 2.1 Compressive stress-strain relationships

In this quasi-static compression experiment, the dotted lattice material exhibits different deformation failure behaviour due to different shapes of the dotted lattice material crystal cells. Fig. 11 shows the compressive stress-strain curves of the dotted lattice structure of  $1 \text{ mm}^3$ . The compressive stress-strain curve of the G7 lattice structure shows four stages: the linear elastic stage, the plateau stage, densification stage and failure stage, similar to the ductile metal foam material, which exhibits the properties of the porous structure of the elastomeric material. In the linear elastic stage, the strain and stress values rise in a linear manner, followed by the plateau stage, where the stress-strain curve enters a slowly rising stage, with a large change in strain and a slight increase in stress. Since the G7 structure is mainly supported by inclined rods, combined with the experimental observation and curve, in this stage the sample is dominated by local plastic deformation. In the densification stage, the G7 structure is continuously compressed, the lattice of each layer begins to stack together uniformly, the stress rises continuously with the compression of the sample, the structure is continuously densified, and continuously plastically deformed, finally local cracks appear, the structure fails, so the structure is a porous structure dominated by tension. The compressive stress-strain curves of the hollow cubic and bcc structures are similar and both go through three stages: the linear elastic stage, the strengthening stage, and the failure stage. Both lattice structures begin with the bending of the struts, leading to elastic deformation, and because of the support of the oblique struts in the bcc, its elastic strain range is larger than that of the hollow cubic structure and its toughness is better; then the curve rises into the strengthening stage slowly and begins to yield. Finally, the curve suddenly

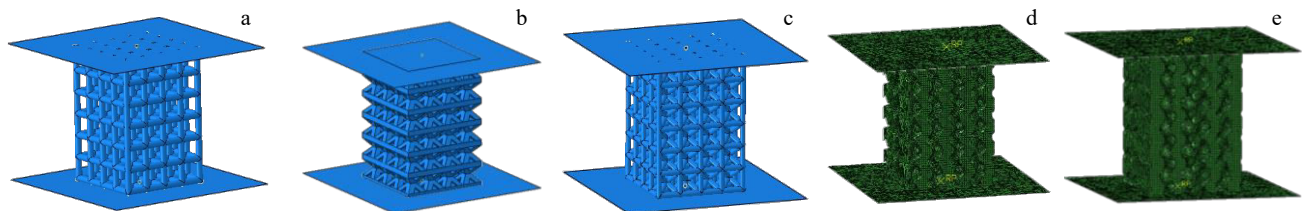


Fig.9 Quasi-static compression model of porous structures: (a) hollow cube, (b) G7, (c) bcc, (d) homogeneous Gyroid, and (e) gradient Gyroid

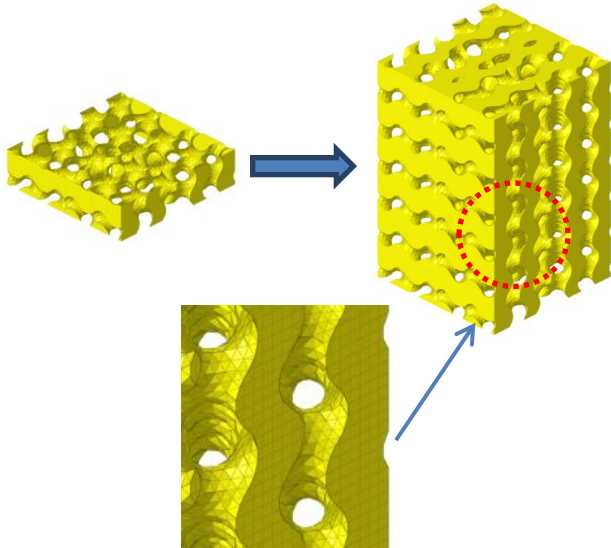


Fig.10 Meshing of the G gradient model

drops and the struts fracture. The graph shows that the smallest fluctuation in the curve of the hollow cubic structure is throughout the compression process, indicating that the hollow cubic structure is a collapse type of fracture, while the G7 and bcc structures have smooth curves and belong to a more stable gradual failure.

The compressive stress-strain curve of the G homogeneous structure shows the typical mechanical response of the porous structure of an elastomeric brittle material. The beginning of compression is a linearly rising linear-elastic phase. When the maximum critical stress that the G homogeneous can

withstand is reached, it enters the plateau structure, and the local cell starts to deform plastically or even collapse, which is an irrecoverable deformation. The stress varies up and down within a certain interval, and finally the upper and lower cells keep stacking together and touching with each other, entering the densification stage, where the stress-strain curve rises continuously and exceeds the maximum stress of the linear elastic zone. The G gradient structure also goes through stages similar to G homogeneous, but since the stress suffered during the compression process is already less than 50% of the maximum stress during the platform stage, the equipment judges that the compression is stopped when the machine decides that the sample has failed.

When the five dotted structures of the single cells are scaled up, their porosity is still guaranteed to be the same and the mechanical response they exhibit is very different. The corresponding phases through which their stress-strain curves are obtained do not change, but their mechanical properties are significantly altered, and their maximum compressive strengths are all decreased accordingly by 26.8%, 11.4% and 61.9% for the hollow cubic, G7 and bcc of the truss-like dot matrix structure, respectively (where G7 is estimated in terms of yield strength), and by 26.5% and 27.7% for the G homogeneous and G gradient of the very small curved dot matrix structure, respectively, with the bcc structure showing the greatest decrease. The compression properties of these five different dot matrix structures are summarized in Table 1. For the samples of 2.5 mm<sup>3</sup> single cells, the Gyroid structure of the very small surface class with similar porosity is superior to the truss-like dot matrix structure, possessing a higher compressive strength, but its elastic modulus is correspondingly

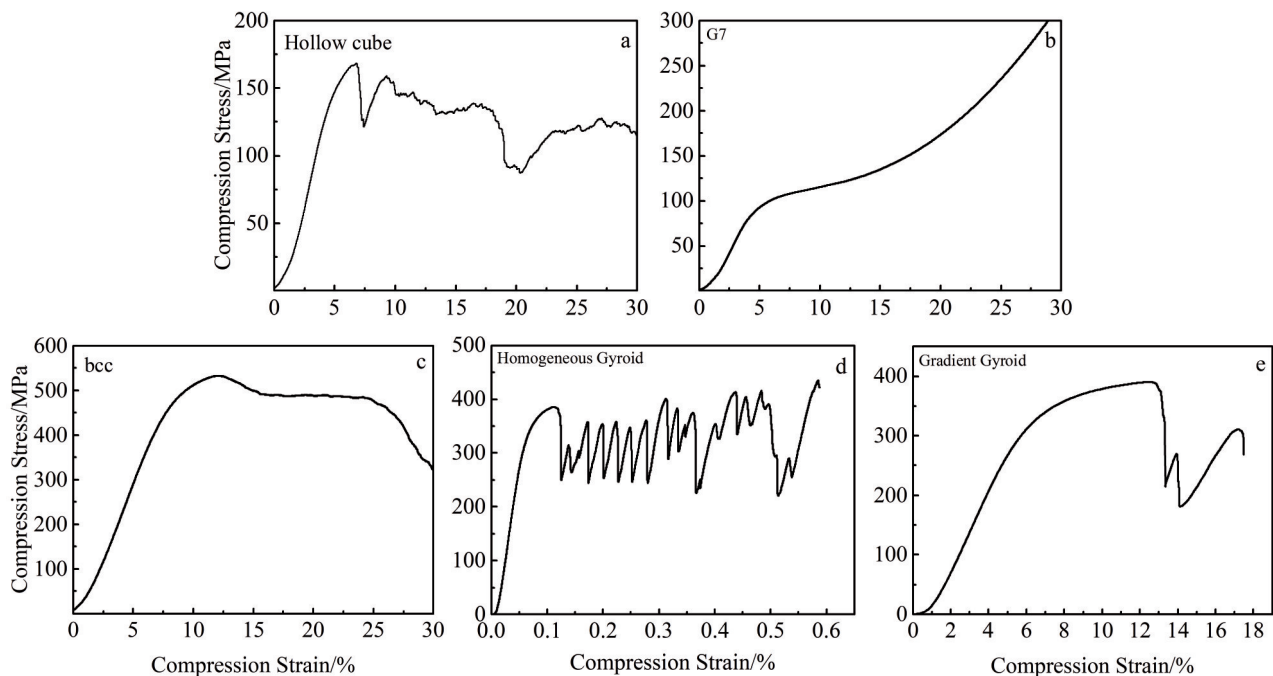


Fig.11 Compressive stress-strain curves of different porous structures (1 mm×1 mm×1 mm single cell composition): (a) hollow cube, (b) G7, (c) bcc, (d) homogeneous Gyroid, and (e) gradient Gyroid

**Table 1** Compression properties of different porous structures

Single cell	Unicellular structure	Maximum compressive strength/MPa	Compressive modulus of elasticity/GPa	Yield strength/MPa
1 mm×1 mm×1 mm	Hollow cube	168	3.96	142
	G7	-	2.64	175
	bcc	530	6.98	450
	G homogeneous	385	7.08	289
	G gradient	390	6.7	298
2.5 mm×2.5 mm×2.5 mm	Hollow cube	123	3.79	106
	G7	-	4.15	155
	bcc	202	4.06	149
	G homogeneous	281	6.27	209
	G gradient	283	5.5	213
	Human bones	-	2–20	-

higher. It seems to be a trend that the higher the maximum compressive strength, the higher the elastic modulus. The maximum compressive strength of the G homogeneous structure is 28% greater than that of the bcc structure, and its modulus of elasticity is correspondingly increased by 35%. It is worth noting that in the comparison between G homogeneous and G gradient, the maximum compressive strength of the G gradient is slightly greater than the maximum compressive strength of the corresponding G homogeneous sample for both 1 mm<sup>3</sup> cells and 2.5 mm<sup>3</sup> cells, while the corresponding modulus of elasticity is reduced by 5%–12%, indicating that the gradient distribution design method achieves higher strength while further reducing the modulus of elasticity and is a very promising approach. The modulus of elasticity of the five porous materials is much lower than that of the solid Ti6Al4V (110 GPa) and is within the range of the

modulus of elasticity of human bone. bcc and Gyroid structures show good compressive and yield strengths and high modulus of elasticity, making them suitable as implants for heavily loaded, dense bone areas. The G7 structure has a very low modulus of elasticity and yield strength better than that of the hollow cube, making it suitable for implants bearing low loads and with low bone density.

**2.2 Stress distribution and plastic deformation of different porous structures**

The equivalent force clouds for the hollow cube, G7, bcc, G homogeneous and G gradient in the linear elastic range were analyzed separately, as shown in Fig.12 (where the stress units are Pa for G homogeneous and G gradient, and MPa for hollow cube, G7 and bcc due to the conversion of units from Hypermesh to ABAQUS), all of which are in a state where plastic deformation is imminent but still in the linear elastic

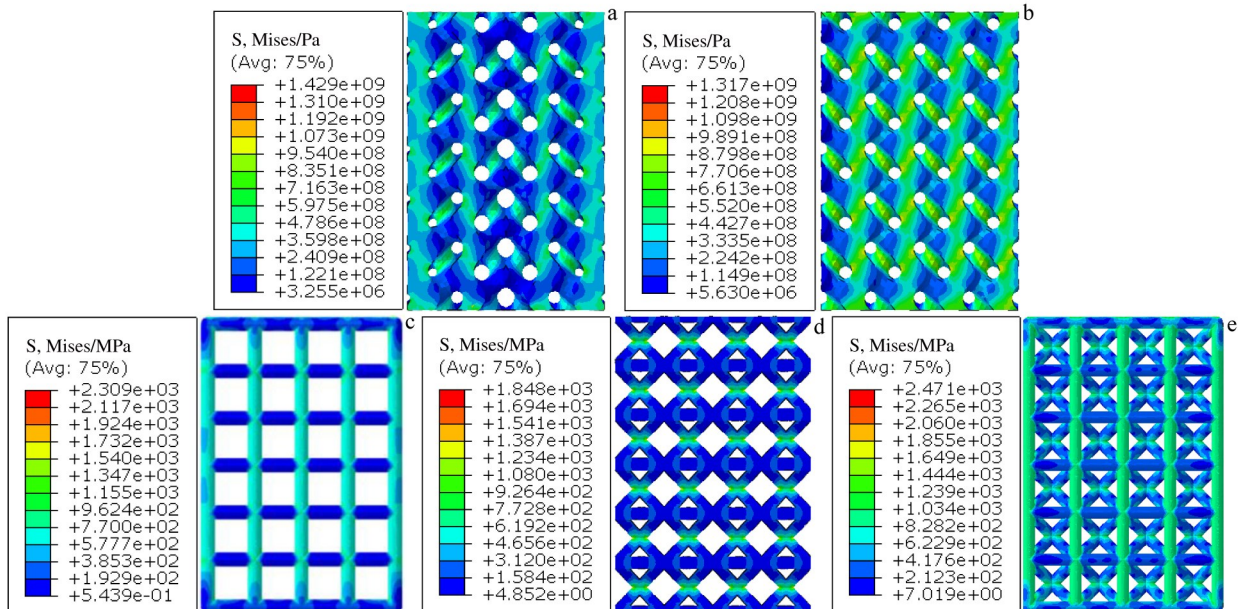


Fig.12 Nephograms of equivalent stress in elastic regions of different lattice structures: (a) G gradient, (b) G homogeneous, (c) hollow cube, (d) G7, and (e) bcc

phase. The G homogeneous model has a uniform distribution of stresses, with no obvious areas of stress concentration, and the stress range of the structure at this point is from 5.63 MPa to 989 MPa. The G gradient model is subjected to higher stresses at the outer low porosity and bears a larger load. The middle part with the lowest porosity bears the least load, at this time the structure is subjected to stresses ranging from 3.255 MPa to 954 MPa. Compared to the G homogeneous structure, they both have similar stress distribution areas, and the minimum and maximum stresses subjected to the G gradient model are smaller than those of the G homogeneous model, indicating that the gradient distribution in the radial direction is conducive to reducing the stresses. As the compression becomes greater, the compressive stresses on the oblique surface begin to transform into tensile stresses, and eventually the tensile stresses reach their ultimate strength and the structure fractures. The point structure of the hollow cube is most likely to cause stress concentration. As can be seen from the numerical graph of stresses, the range of its stress distribution is the largest, the distribution of forces is not uniform, so it should be avoided as far as possible in the design and application of similar structures. The G7 structure is better than the hollow cubic structure, although it can resist large deformation and is not easy to fracture, because of the easy force at the intersection of the diagonal struts where plastic deformation is easy to occur, at the expense of the maximum compressive strength. The bcc structure stress distribution range is better than the hollow cubic structure and the G7 structure is not as good as the Gyroid structure, and the vertical support struts share part of the diagonal struts. In the

process of continuous downward pressure, as the bcc lattice deforms, compressive stresses begin to change to tensile stresses at the horizontal and vertical struts, and eventually fracture occurs here.

By comparing the plastic strain clouds of these five point structures with the failures occurred during the experimental process, the failure deformation process of these five structures is analyzed and the correctness of this finite element analysis is verified again. As shown in the plastic strain cloud of the G gradient dot matrix structure in Fig. 13a, it is obvious from the experimental photograph that a line of mutually parallel oblique cracks are produced on the right side, which is precisely due to the cracks after excessive plastic deformation. From the simulation results, the plastic strain on the right side of the simulation model is also the largest at the corresponding place, and the plastic strain starts first at the outermost layer of the structure. At the minimum porosity, as the compression continues, the plastic deformation expands from the outer side to the inner side, and the G gradient model has the tendency to retard the expansion of the plastic strain to the inner side. As shown in Fig. 13b, the distribution of failure in G homogeneous during compression is consistent with the site of maximum plastic strain in the simulation results. The model in the online elastic phase is mainly subjected to axial squeezing force and compressive stresses, and after entering the plastic phase, tensile stresses keep appearing at the inclined surface, and the maximum tensile stresses are found at the fracture, which eventually lead to the fracture of the structure. As shown in Fig. 13c, the simulated deformation failure of the hollow cubic structure agrees exactly with the

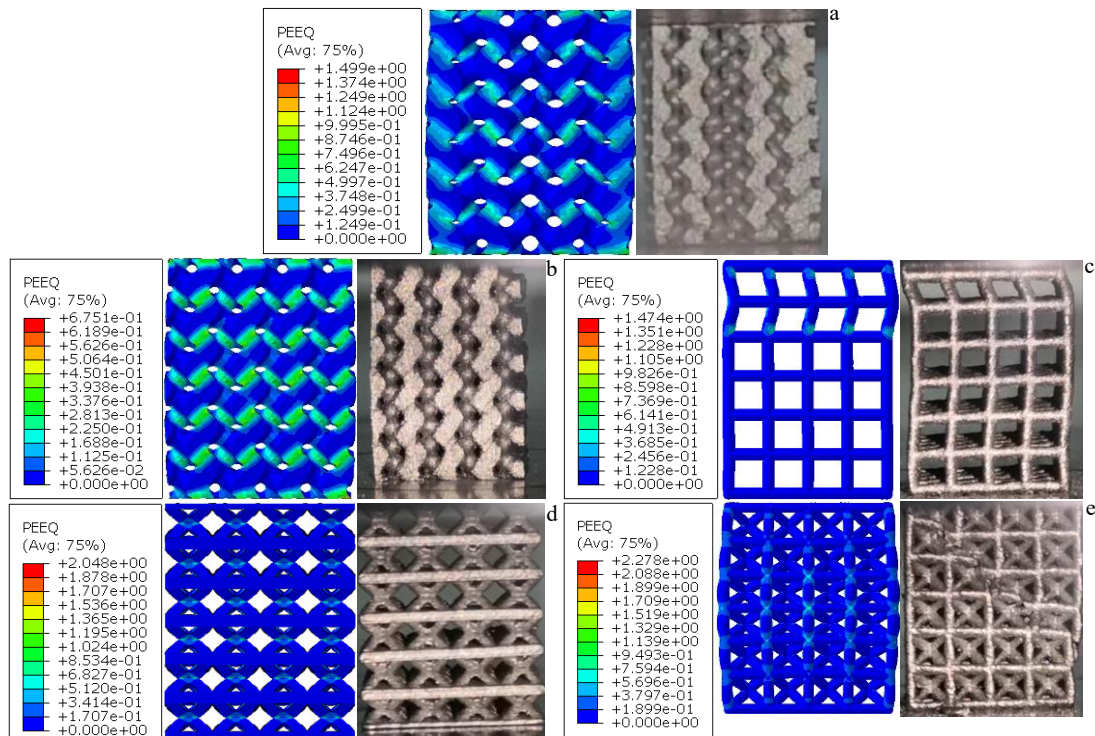


Fig. 13 Plastic strain cloud diagram of different lattice structures: (a) gradient Gyroid, (b) homogeneous Gyroid, (c) hollow cube, (d) G7, and (e) bcc

experimental phenomenon. The upper two layers of the lattice first fracture. As shown in Fig. 13d, the G7 structure is uniformly compressed, and as the plastic deformation of the cross struts increases, it causes the struts to produce small rotations, generating plastic hinges that break the otherwise uniform forces, thus also explaining the crack extension along the 45° direction that occurs in the G7 structure after a plateau phase. As shown in Fig. 13e, the bcc structure is supported by the vertical strut, which shares part of the pressure. The plastic strain at the intersection of the two inclined struts is small, which to a certain extent limits the generation of plastic hinges at the strut intersection, and the plastic deformation is the first to fracture at the maximum amount of plastic deformation, and the simulation is consistent with the experimental phenomenon. After the vertical column has reached its yield strength, the inclined column starts to take the main pressure and the plastic hinge begins to develop. This explains why the stress-strain curve obtained from the experiments for the central cubic structure does not drop as steeply as that for the hollow cubic structure, but gently with a plateau phase after the first drop, which is due to the pressure supported by the inclined column.

The corresponding force versus displacement curves were extracted from the simulation model and plotted as stress-strain curves for comparison with the experimentally derived data, as shown in Fig. 14. As the simulation model is compressed under ideal conditions, the compressed sample is made in full stable contact and the model enters the linear elastic region directly, whereas in the experiment the sample is not in full contact with the upper platen, so the downward

compression process will go through a region of initial contact before entering the linear elastic phase. As shown in Fig. 14a and 14b, the simulated models of G gradient and G homogeneous keep densifying after reaching the yield strength and cannot simulate fracture, so the stresses rise steadily and the maximum compressive strengths are 322 and 305 MPa, respectively when the models enter the stable densification stage. Due to the complex geometric configuration and manufacturing process of TPMS, the simulated and experimental results of mechanical properties cannot be fully consistent. However, the trend is consistent with the experimental results, and the maximum compressive strength of the G gradient from the simulation results is also slightly greater than that of the G homogeneous.

As shown in Fig. 14b–14d, the simulation results for the hollow cubic, G7, bcc structure are smaller than the experimental results, and there are four main reasons for such results. (1) SLM machining of such truss-like structures will result in low quality machining and the thickness of the struts will be slightly thicker than that of the model struts. (2) During the experiments, the metal struts will have a certain strengthening stage during the compression process, which also makes the experimental results slightly larger than the simulation results. (3) Bone scaffolds prepared by SLM are typically thin-walled and thus have a slightly lower density than dense parts, resulting in reduced mechanical properties, which is consistent with the findings of Vilardell et al.<sup>[24]</sup> (4) In this study, we obtain bone scaffolds with different porosities by keeping the wall thickness constant and varying the pore size, so the larger the porosity, the larger the corresponding

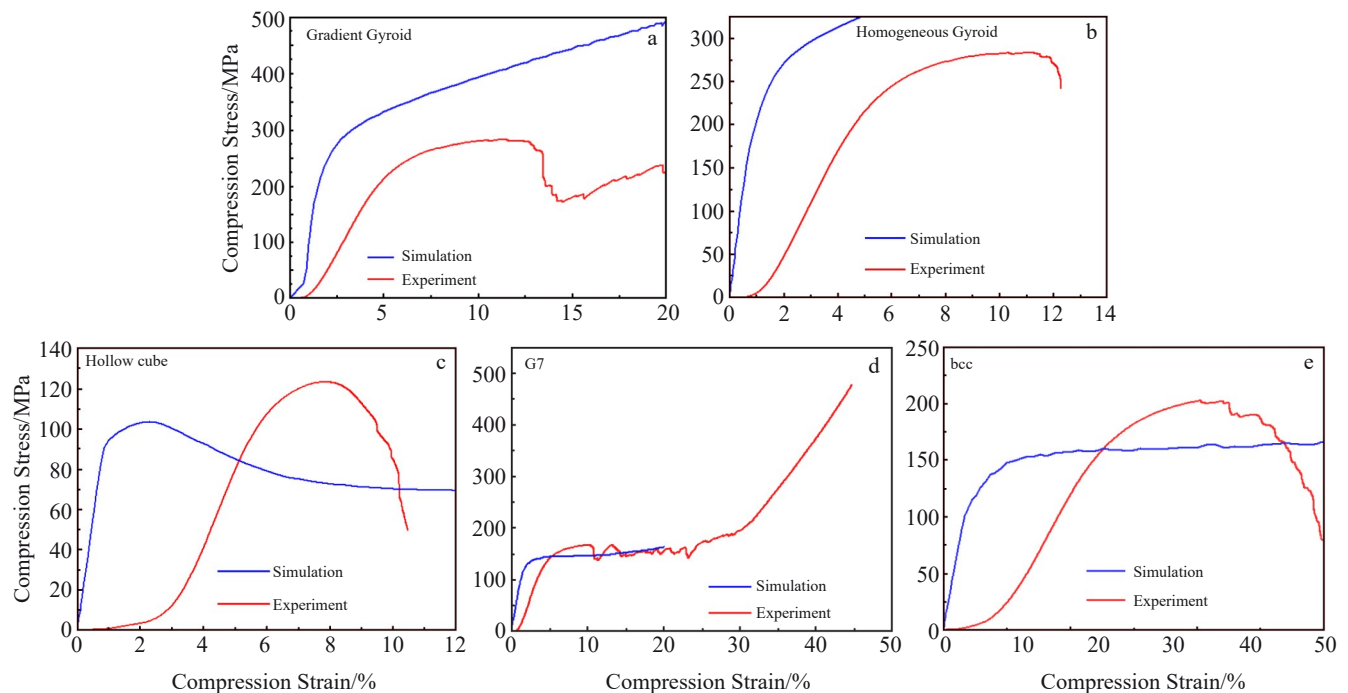


Fig.14 Comparison of simulation and experimental compressive stress-strain curves: (a) gradient Gyroid, (b) homogeneous Gyroid, (c) hollow cube, (d) G7, and (e) bcc

cell size, and there will be a longer overhanging part, which will lead to more manufacturing defects and thus weaken the mechanical properties of the bone scaffold. This is also in agreement with the conclusion of Xu et al.<sup>[25]</sup>. Therefore, the difference in the simulation and experimental results is acceptable. Taken together, the method can basically predict the general trend of the stress-strain curves of different structures and their maximum compressive strength when predicting the compression properties of each porous structure, which can effectively reduce the number of experiments and reduce the cost of experiments.

### 2.3 Tensile properties

Since porous implants are often subjected to tensile loading, tensile tests were performed and the results show similar tensile properties for homogeneous and gradient Gyroid structures. After the tensile forces exceed their yield limit, a long hardening phase is entered. During this phase the resistance of the materials to deformation increases until their ultimate strength is exceeded, and then the samples fracture. The experimental results show that the maximum tensile strength of the gradient Gyroid is slightly higher than that of the homogeneous Gyroid structure (282.9 MPa) at 285.5 MPa, and the corresponding strain is 1.42% higher than that of the homogeneous Gyroid structure (1.32%), thus indicating that the Gyroid structure with a radial gradient distribution at the same porosity has slightly better tensile properties than the homogeneous Gyroid.

## 3 Conclusions

1) Five types of unicellular structures are designed and studied, and the TPMS-like model designed by MATLAB can accurately control the relative volume and gradient distribution of single cells.

2) The Gyroid structure is basically free of bonded metal blobs and has better molding accuracy, indicating that the TPMS structure is more suitable for the SLM processing process.

3) In terms of mechanical properties, the Gyroid structure exhibits good compressive properties, and the gradient Gyroid structure has higher compressive strength and lower elastic modulus than the homogeneous Gyroid structure. Both experimental and simulation results show that the G gradient structure has the best overall mechanical properties.

## References

- 1 Li Xiang, Wang Chengtao, Wang Lin et al. *Rare Metal Materials and Engineering*[J], 2010, 39(10): 1697
- 2 Yavari S A, Wauthle R, Van Der Stok J et al. *Materials Science & Engineering C, Materials for Biological Applications*[J],

- 2013, 33(8): 4849
- 3 Wang Maohua, Duan Mingde, Yang Ziwei et al. *Mechanical Strength*[J], 2022, 44(2): 424 (in Chinese)
- 4 Li Xuejing, Qiu Xiaohai, Zhao Baohong. *Chinese Journal of Practical Dentistry*[J], 2020, 13(8): 501 (in Chinese)
- 5 Branemark P I, Breine U, Adell R et al. *Plastic and Reconstructive Surgery*[J], 1971, 48(1): 97
- 6 Lu Bingheng, Li Dichen. *Machine Manufacturing and Automation*[J], 2013, 42(4): 1 (in Chinese)
- 7 Kietzmann J, Pitt L, Berthon P. *IEEE Engineering Management Review*[J], 2015, 58(2): 209
- 8 Baumers M, Dickens P, Tuck C et al. *Technological Forecasting and Social Change*[J], 2016, 102: 193
- 9 Ford S, Despeisse M. *Journal of Cleaner Production*[J], 2016, 137(20): 1573
- 10 Ian Gibson, David Rosen, Brent Stucker. *Additive Manufacturing Technologies-3D Printing, Rapid Prototyping, and Direct Digital Manufacturing*[M]. New York: Springer, 2009
- 11 Shipley H, McDonnell D, Culleton M et al. *International Journal of Machine Tools and Manufacture*[J], 2018, 128: 1
- 12 Murr L E. *Journal of the Mechanical Behavior of Biomedical Materials*[J], 2017, 76(S1): 164
- 13 Zadpoor Amir A. *Biomaterials Science*[J], 2015, 3(2): 231
- 14 Xiang Zheng, Chen Jie, Yang Qin et al. *Rare Metal Materials and Engineering*[J], 2022, 51(11): 10
- 15 Ferry P W Melchels, Katia Bertoldi, Ruggero Gabbriellini et al. *Biomaterials*[J], 2010, 31(27): 6909
- 16 Zadpoor A A. *Biomaterials Science*[J], 2015, 3(2): 231
- 17 Olivares A L, èlia Marsal, Planell J A et al. *Biomaterials*[J], 2009, 30(30): 6142
- 18 Afshar M, Pourkamali Anaraki A, Montazerian H. *Materials Science & Engineering C*[J], 2018, 92: 256
- 19 Jga B, Jian H C, Yi B et al. *Surface and Coatings Technology*[J], 2020, 403: 126 419
- 20 Fukuda A, Takemoto M, Saito T et al. *Acta Biomaterialia*[J], 2011, 7(5): 2327
- 21 Zargarian A, Esfahanian M, Kadkhodapour J et al. *Materials Science & Engineering C Materials for Biological Applications*[J], 2016, 60: 339
- 22 Campoli G, Borleffs M S, Yavari S A et al. *Materials & Design*[J], 2013, 49: 957
- 23 Khaderi S N, Deshpande V S, Fleck N A. *International Journal of Solids and Structures*[J], 2014, 51(23–24): 3866
- 24 Vilardell A M, Takezawa A, Du Plessis A et al. *Materials Science and Engineering A*[J], 2019, 766: 138 330
- 25 Xu Y, Zhang D, Zhou Y et al. *Materials*[J], 2017, 10(9): 1048

## 桁架类与极限曲面类点阵结构的力学性能

张建国<sup>1</sup>, 王冠<sup>1</sup>, 陈朋<sup>1</sup>, 赵晟<sup>1</sup>, 胡凤玲<sup>2,3</sup>, 宋亮<sup>4</sup>, 周琼<sup>1</sup>, 张而耕<sup>1</sup>

(1. 上海应用技术大学 机械工程学院 上海物理气相沉积 (PVD) 超硬涂层及装备工程技术研究中心, 上海 201418)

(2. 上海市老年医学中心, 上海 201100)

(3. 复旦大学附属中山医院口腔科, 上海 200032)

(4. 复旦大学附属上海市第五人民医院口腔科, 上海 200240)

**摘要:** 多孔钛合金的设计与力学性能是生物医学领域的研究热点。通过SLM技术设计并制造了2种均质和梯度的Gyroid极小曲面单胞结构, 通过对其进行静态压缩试验和拉伸试验并与传统的桁架类单胞结构做对比, 建立了5种不同点阵结构的准静态压缩模型。通过Hypermesh与ABAQUS联合仿真的方式, 对它们进行了网格划分与分析计算, 通过应力应变云图、塑性应变云图以及压缩实验过程的观察, 综合分析了空心立方、G7、bcc、均质Gyroid和梯度Gyroid 5种多孔结构失效形式和变形机制, 将仿真得出的应力应变曲线与试验结果进行了对比, 发现该仿真方法可以较好预测出不同多孔结构的最大抗压强度。压缩和拉伸试验结果表明, Gyroid点阵材料的最大抗拉性能远高于桁架类结构, 抗压性能也更优越。其中, G梯度结构的综合力学性能最优。

**关键词:** 激光选择性熔化; Ti6Al4V合金; 三周期最小表面; 有限元分析

**作者简介:** 张建国, 男, 1979年生, 博士, 副教授, 上海应用技术大学机械工程学院, 上海物理气相沉积 (PVD) 超硬涂层及装备工程技术研究中心, 上海 201418, E-mail: jianguozhang@sit.edu.cn